Development and Ex Vivo Validation of Novel Force-Sensing Neochordae for Measuring Chordae Tendineae Tension in the Mitral Valve Apparatus Using Optical Fibers With Embedded Bragg Gratings

Michael J. Paulsen
Department of Cardiothoracic Surgery,
Stanford University,
Stanford, CA 94305
e-mail: mpaulsen@stanford.edu

Jung Hwa Bae
Department of Mechanical Engineering,
Stanford University,
Stanford, CA 94305
e-mail: jbae7@stanford.edu

Annabel M. Imbrie-Moore
Department of Cardiothoracic Surgery,
Stanford University,
Stanford, CA 94305;
Department of Mechanical Engineering,
Stanford University,
Stanford, CA 94305
e-mail: aimbrie@stanford.edu

Hanjay Wang
Department of Cardiothoracic Surgery,
Stanford University,
Stanford, CA 94305
e-mail: hanjay@stanford.edu

Camille E. Hironaka
Department of Cardiothoracic Surgery,
Stanford University,
Stanford, CA 94305
e-mail: chironak@stanford.edu

Justin M. Farry
Department of Cardiothoracic Surgery,
Stanford University,
Stanford, CA 94305
e-mail: justinfarry@stanford.edu

Haley Lucian
Department of Cardiothoracic Surgery,
Stanford University,
Stanford, CA 94305
e-mail: hlucian@stanford.edu

Akshara D. Thakore
Department of Cardiothoracic Surgery,
Stanford University,
Stanford, CA 94305
e-mail: athakore@stanford.edu

Mark R. Cutkosky
Department of Mechanical Engineering,
Stanford University,
Stanford, CA 94305
e-mail: cutkosky@stanford.edu

Y. Joseph Woo[1]
Norman E. Shumway Professor and Chair
Department of Cardiothoracic Surgery,
Stanford University,
Stanford, CA 94305;
Department of Bioengineering,
Stanford University,
Stanford, CA 94305
e-mail: joswoo@stanford.edu

Few technologies exist that can provide quantitative data on forces within the mitral valve apparatus. Marker-based strain measurements can be performed, but chordal geometry and restricted optical access are limitations. Foil-based strain sensors have been described and work well, but the sensor footprint limits the number of chordae that can be measured. We instead utilized fiber Bragg grating (FBG) sensors—optical strain gauges made of 125 μm diameter silica fibers—to overcome some limitations of previous methods of measuring chordae tendineae forces. Using FBG sensors, we created a force-sensing neochord (FSN) that mimics the natural shape and movement of native chordae. FBG sensors reflect a specific wavelength of light depending on the spatial period of gratings. When force is applied, the gratings move relative to one another, shifting the wavelength of reflected light. This shift is directly proportional to force applied. The FBG sensors were housed in a protective sheath fashioned from a 0.025 in. flat coil, and attached to the chordae using polytetrafluoroethylene suture. The function of the force-sensing neochordae was validated in a three-dimensional (3D)-printed left heart simulator, which demonstrated that FBG sensors provide highly sensitive force measurements of mitral valve chordae at a temporal resolution of 1000 Hz. As ventricular pressures increased, such as in hypertension, chordae forces also increased. Overall, FBG sensors are a viable, durable, and high-fidelity sensing technology that can be effectively used to measure mitral valve chordae forces and overcome some limitations of other such technologies.
[DOI: 10.1115/1.4044142]

Introduction

In the U.S., valvular heart disease is a common cause of morbidity and mortality, with an estimated 2.5% of the population affected [1]. In large epidemiologic natural history studies, projected 5 and 8 yr survival rates for individuals suffering from valvular heart disease is 79% and 68%, respectively, rivaling that of many types of cancer. The most prevalent type of valvular heart disease is degenerative or myxomatous mitral regurgitation, with nearly 2% of the U.S. population suffering from at least moderate mitral regurgitation [1–5]. Of these patients, approximately 10% progress to severe mitral regurgitation requiring surgery [6–9]. Mitral valve repair is the preferred treatment for degenerative mitral regurgitation [10]. As compared to valve replacement with a bioprosthetic or mechanical valve, an effective and durable

[1]Corresponding author.
Manuscript received August 10, 2018; final manuscript received May 23, 2019; published online October 1, 2019. Assoc. Editor: Jeffrey Ruberti.

mitral valve repair procedure improves patient survival, preserves left ventricular function, and results in greater freedom from reoperation [11–16]. However, the key part of this statement is "effective and durable" as many surgeons lack the knowledge or ability to perform this type of repair; as such, a large subset of patients with degenerative mitral disease still undergo replacement over repair [17,18].

The mitral valve apparatus is a dynamic and intricate structure that is comprised of two leaflets (anterior and posterior); the atrioventricular junction and annulus connecting the leaflets to the walls of the heart; and the subvalvular apparatus. The subvalvular apparatus consists of long fibrous supports called chordae tendineae, which anchor the leaflets to the papillary muscles and left ventricular free wall. Dysfunction of any of these components can result in valve incompetence and resultant mitral regurgitation. To succeed in repairing a dysfunctional mitral valve, a comprehensive understanding of the mitral valve apparatus spatial geometry is mandatory. Even with this knowledge, however, mitral valve repair is challenging and our understanding of how exactly the mitral valve functions is incomplete. Clouding this further is the existence of a multitude of mitral repair techniques, with little to no consensus or objective physiological data suggesting which repair technique is superior. The ability to quantitatively measure structural data, such as chordae tendineae tension, without adversely impacting leaflet motion, would generate a more comprehensive understanding of mitral valve pathology and how best to treat it.

Very few technologies exist that can provide quantitative data on forces within the mitral valve complex. Echocardiography can generate extremely useful, and increasingly high-fidelity, estimates of strain and forces within the mitral valve apparatus, but may be limited by tissue penetration and the inability to make direct measurements [19–23]. Although marker-based strain measurements can be performed to analyze the chordae tendineae, the narrow thickness and small strains relative to the spatial resolution of the current marker-based optical technology may present significant sources of error, particularly for the primary chordae. Additionally, the restricted optical access and branching patterns of the chordae limit the utility of this technique in vivo. While advancements in machine vision technology and image processing algorithms have made automated analysis of marker-based optical strain measurements substantially faster and more reliable, manual correction and verification remains necessary and time-consuming. Small C-shaped force transducers have been described and used to measure transverse chordae tendineae tension both in vitro and in vivo [24–31]. These transducers have been shown to be reliable and provide high-quality data. A potential limitation, however, is their relatively large footprint relative to the size of the chordae tendineae, which minimizes the number of chordae that may be instrumented simultaneously. Additionally, the transducers have a high mass relative to the chordae, which might interfere with normal chordal motion. The use of miniaturized arthroscopically implantable force probes (AIFP4) for measuring chordal forces has also been described, whereby a small slit is made in the chordae and the elliptical sensor is inserted perpendicularly to measure transverse strain through a cantilever-type mechanism [32]. While this method minimizes the sensor footprint, measurement errors can occur if the sensor shifts from perpendicular alignment. In addition, this technique also requires that a slit large enough to accommodate the 1.8 mm diameter sensor be made in the chordae longitudinally, which limits sensor implantation to only larger chordae. Finally, these force sensors are no longer available commercially. In this study, we describe the use of fiber Bragg grating (FBG) sensors—optical strain gauges made of 125 μm diameter silica fibers—to overcome some limitations of previous methods for measuring chordae tendineae forces.

Methods

Force-Sensing Neochord. We developed a force-sensing neochord (FSN) that mimics the natural shape and movement of natural chordae tendineae as much as possible to overcome some limitations of prior chordae force transducers. The force-sensing neochord consisted of an optical strain gauge and attachment method. We chose to use FBG sensors to measure forces in our force-sensing neochord.

Fiber Bragg Grating Optical Strain Sensors. Fiber Bragg grating sensors are a type of optical strain gauge. When a spectrum of light passes through the optical fiber, the FBG sensor reflects a specific wavelength of light depending on the spatial period of gratings (Fig. 1(*a*)). When force is applied on the sensor, the sensor portion of the optical fiber is strained, increasing the distance between gratings. Force-induced strain of the FBG sensor is then detected as a wavelength shift (Fig. 1(*b*)). Temperature change can also cause a wavelength shift as shown in the following equation:

$$\Delta\lambda = K_\varepsilon \varepsilon + K_T \Delta T \tag{1}$$

where $\Delta\lambda$ is the wavelength shift, K_ε is the constant for mechanical strain, ε is the mechanical strain, K_T is the constant for temperature, and ΔT is the change in temperature. The optical fiber with embedded FBG sensors is waterproof, facilitating implementation of the chordae in a fluid-filled test chamber while the interrogator that reads the wavelength can remain outside of the chamber. Additionally, FBG sensors are very sensitive to mechanical strain; the minimum strain the sensor can resolve is approximately 0.1 microstrain [33].

Design and Fabrication of the Force-Sensing Neochord. Unlike foil strain gauges, FBG sensors can be used without any base structure to attach the strain gauges. The FBG sensor fiber (DTG-LBL-1550 125 μm FBGS International, Geel, Belgium) can be the base structure itself, as it is strong enough to sustain newtons of tensile force. With no base structure, we can achieve maximum force sensitivity from the FBG sensor as well as a lightweight and compact final sensing unit that reduces noise due to inertia of the base structure in dynamic force reading. The process for manufacturing the neochord sensors as well as various prototype iterations is shown in Fig. 1. In our first iteration, we tied and glued two double-armed polytetrafluoroethylene sutures (Gore-Tex® CV-7 Suture, W. L. Gore & Associates, Inc., Flagstaff, AZ) just proximal and distal to the 8 mm FBG sensor using cyanoacrylate (Fig. 1(*b*)). Two square knots were tied prior to gluing and demonstrated secure bonding up to 4 N. The sutures were then used to secure the sensor to the chordae tendineae of interest with great care taken to ensure that the native length was preserved and not affected by sensor implantation. Nonetheless, small imperfections in the resultant length of the instrumented chordae represent a limitation of this model given that changes in chordal length could affect the measured loads. First, the proximal suture was attached to the chordae distal to the chordae's papillary muscle insertion; any bunching or stretching of the chord due to small misalignments (which could ultimately affect the final length of the instrumented chordae) were corrected by shifting the FBG up or down to return the chordae to its native state. The other end of the FBG sensor was then attached to the chordae proximal to the leaflet insertion point and the chordae were severed between attachment points, loading the forces to the sensor. It was important to leave some length of chordae intact proximally and distally to the fiber attachment points to retain the material properties of the chordae, given that the elastic modulus of the fiber sensor is several hundred times greater than that of a typical chordae. Initially, the FBGs were manufactured to be 8 mm in length, though we eventually reduced this length to 3 mm overall; as the length decreases and the sensor replaces a smaller section of the chordae, the stiffness of the instrumented chordae converges to the native stiffness. The effect of fiber stiffness relative to chordae stiffness, and its effect on sensor error, is discussed more fully in the Error Estimation section below. While the first prototype performed extremely well, a critical limitation was the difficulty in reusing the fibers

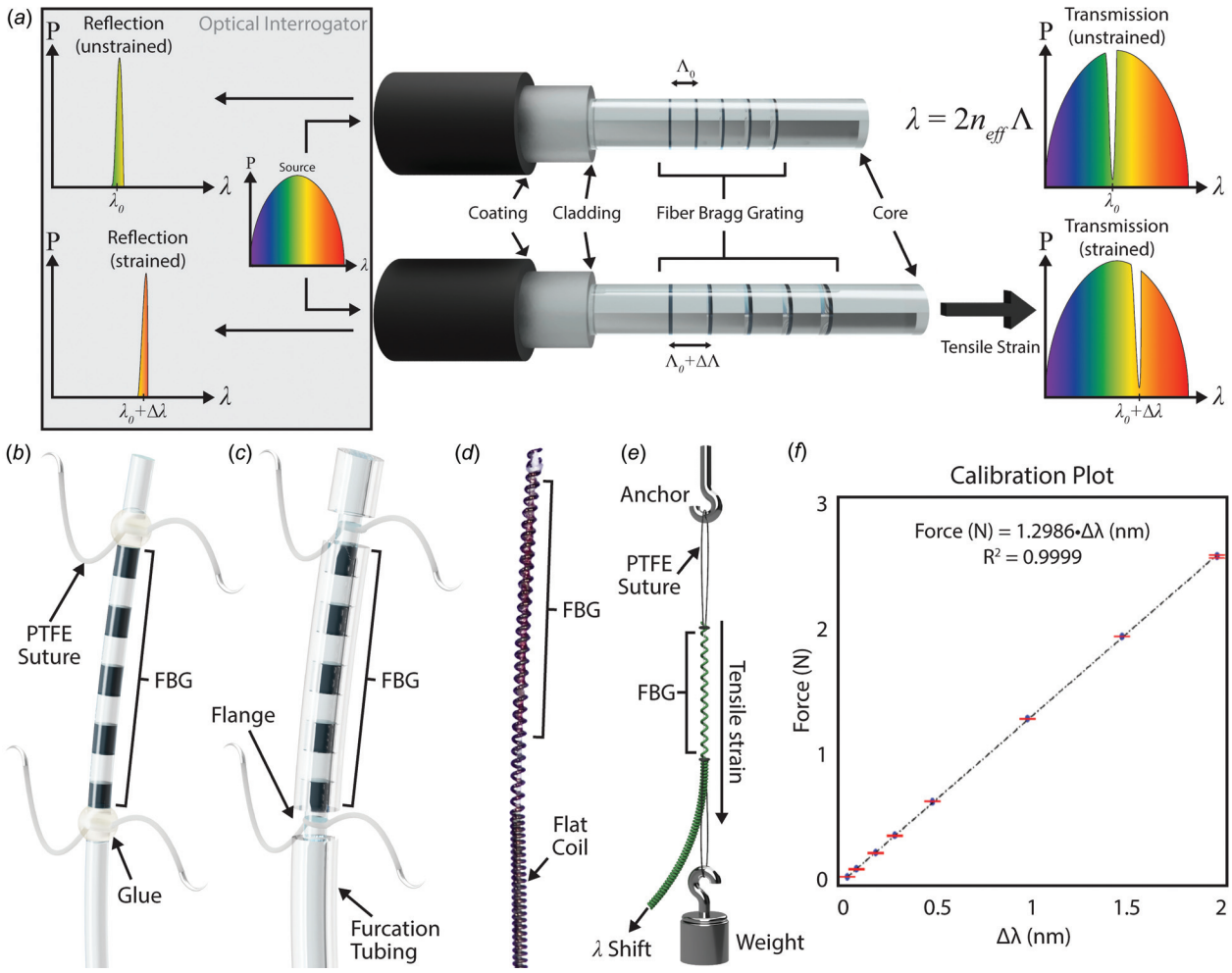

Fig. 1 Principles of fiber Bragg grating operation (*a*) demonstrating wavelength shift when tensile or compressive force applied. Initial prototype (*b*) with PTFE suture tied and glued directly to a naked fiber proximal and distal to the FBG. Second prototype (*c*) whereby suture-holding flanges are created with furcation tubing glued to the fiber, leaving small gaps proximal and distal to the fiber; suture are not glued directly to the fiber for easier reuse. Final prototype (*d*) where FBG is secured inside of an expanded flat coil, which serves to capture suture similar to a flange design but with a lower profile and more protection of the fiber. (*e*) Schematic of calibration setup using known weights. (*f*) Example calibration plot relating force in Newton to the change in wavelength.

for subsequent experiments. To do so, it was necessary to dissolve the glue and then retie and reglue the sutures; this was a laborious process and required great care to avoid breaking the fibers.

To make the sensors easier to reuse, flanges on each end of the FBG sensor were fashioned from 900 μm plastic furcation tubing, which was then glued to the fiber, leaving small gaps proximal and distal to the sensor, as shown in Fig. 1(*c*). These flanges served as suture-locking grooves (SLG), achieving a similar suture attachment without the use of glue. In this design, the polytetrafluoroethylene (PTFE) suture sewn to the chordae was tied between the flanges within the suture-locking groove, which kept the fiber securely in place. Depending on the diameter of the chordae, various sizes of PTFE suture can be used, ranging from size CV-5 to CV-7 in these experiments. After the experiment, the suture was cut and easily removed without damaging the sensor. This modified design successfully not only allowed us to reuse the sensors multiple times but also possessed limitations. The bare optical fiber was exposed in the flanges between the furcation tubing, creating a fragile point in the sensor that tended to get caught in the papillary muscle holding mechanism during removal, often resulting in fiber damage.

In our final prototype, we kept the suture-locking groove method for attaching the sensors to the chordae for easy reuse, but fashioned the grooves from a different material—a small 0.025 in. outer diameter flat coil, as shown in Fig. 1(*d*). For early prototypes, we used the outer coil of a vascular access wire, in this case a 0.025 in. Amplatz Extra-Stiff™ guidewire (Cook Medical, Bloomington, IN), which consists of a stainless-steel mandrel covered in a PTFE-coated stainless-steel flat coil. Each end of the wire was cut so that the mandrel could be removed, leaving only the hollow outer coil. On one end, the coil was expanded, creating gaps between the wires. The length of the expanded section was trimmed to 12 mm to accommodate 2 mm for suture attachment on each end of the 8 mm FBG; once the 3 mm FBGs were manufactured, total length of the expanded section was reduced to approximately 7 mm. The FBG fiber, which was prepared beforehand by terminating the fiber 2 mm distal to the end of the FBG, was then carefully passed through the nonexpanded end of the coil until it was flushed with the expanded end of the coil. Cyanoacrylate glue was used to securely bond the FBG to the outer coil, being careful not to use an excessive amount of glue that would fill the gaps between the coils and render it useless as a flange to retain suture. The FSN was attached to the mitral valve chordae in a similar fashion as described in the prior section for the flanged SLG prototype. Further iterations have used customized flat coils with features specific to this implementation as well as an optimized implantation protocol described below.

Calibration. To measure forces on the chordae, the FSN was calibrated using known weights. With one end of the FSN fixed on a stand, weights were applied to the other end of the FSN to apply known calibration forces (Fig. 1(*e*)). The shift in reflected wavelength is linearly proportional to the strain on the FSN, which is linearly proportional to the applied force. Therefore, we can find a linear calibration equation that outputs the force value on the FSN based on the wavelength shift from strain. The wavelength shifts were measured using an optical interrogator (Optical Sensing Instrument si255, 1 kHz sampling rate, Micron Optics, Inc., Atlanta, GA). Fig. 1(*f*) demonstrates how force and wavelength are related, which is also described by the following equation:

$$\Delta\lambda = \left(\frac{K_\varepsilon}{A_{\text{fiber}}E}\right)F_{\text{weight}} + K_T\Delta T \tag{2}$$

where $\Delta\lambda$ is the wavelength shift, K_ε is the constant for mechanical strain, F_{weight} is the force applied to the FBG sensor, A_{fiber} is the cross-sectional area of the fiber, E is Young's modulus of the fiber, K_T is the constant for temperature, and ΔT is the change in temperature. As shown in Eq. (2), temperature influences wavelength as well as force. Since we are primarily interested in force while the temperature ideally remains constant during experimentation, we treat temperature as a source of error. To quantify the magnitude of temperature error on the FSN, they were subjected to temperature changes using a halogen light source and thermocouple to measure temperature changes accurately. We found that at the temperatures and force ranges typically found in the testing environment, the effect of temperature is very small compared to the force: a 1 °C temperature change is equivalent to approximately 0.01 N of force. To minimize error due to temperature fluctuation, temperature of the testing environment was tightly controlled and held constant at 37 ± 0.2 °C, corresponding to a maximum error in the force measurement ranging between 0.2% for the largest chordae being measured to 4% in the smallest chordae measured. The strain sensitivity of our sensors was tested using an Instron 5848 Microtester (Illinois Tool Works, Inc., Norwood, MA) with a 20 N load cell and found to be less than the reported 0.1 microstrain. We also tested the accuracy and sensitivity of our calibration translating measured strains into forces. The accuracy was found to be approximately 3% and the sensitivity 0.01 N, both tested using forces less than or equal to 2 N given that this was the relevant range for this study. Because all forces measured in the mitral valve experiments are relative to the native baseline preload on the chordae, the FBG sensors were zeroed immediately prior to data collection during experimentation, thus mitigating accuracy errors.

Error Estimation. Mismatch between the stiffness of the sensors and the native chordae tendineae is a source of measurement error using this technology, as with other strain gauge technologies. If the chordae tendineae are mechanically coupled and instrumented chordae are notably stiffer than uninstrumented neighboring chordae, the instrumented chordae would carry a disproportionate fraction of total force. However, we posited that our technique of replacing only a small segment of the chordae tendineae with the sensor could help mitigate measurement error to some degree, as the majority of the chordae tissue (with its native viscoelastic material properties) remains intact in the instrumented state. To assess whether this technique does attenuate the differences in stiffness between chordae tendineae and the optical fibers, we performed Instron tensile testing to compare load versus extension between an instrumented and uninstrumented chordae. We measured primary chordae, as they are thinner and shorter than secondary chordae and more likely to be affected by potential changes in stiffness due to sensor instrumentation. Preconditioning occurred at 1 mm/s to 5% strain for 5 cycles, adapted based on existing protocols for measuring chordae tendineae mechanical properties [34,35]. The chordae were then subjected to 5 cycles of 20% strain at 1 mm/s (at which point the stress versus strain cycle was repeatable) and the final cycle was plotted (Supplemental Fig. 1 available in the Supplemental Materials on the ASME Digital Collection). Load versus extension was plotted here rather than the more traditional stress versus strain in order to more accurately compare how differences between the two conditions would impact the validity of the gauge readings when translating the FBG measurements to load on the chordae. This plot demonstrates that instrumented and uninstrumented chordae tendineae display similar slopes (i.e., stiffness) at each stage of the loading and unloading cycle, particularly at points within the load range we observed most force measurements to reside (between 0 N and 1.5 N). In addition, instrumented chordae maintain the classic hysteresis loop (indicating lost energy in the loading cycle) that is associated with biologic, viscoelastic materials. Based on the results of this single pilot experiment to investigate tissue stiffness with and without the sensor, our technique of replacing only a small segment of chordae with the sensor preliminarily appears to help preserve the native stiffness of the instrumented chordae tendineae, which may minimize measurement error due to alternations in chordae material properties following sensor implantation. Furthermore, the fact that the tissues bracketing each chordae (the leaflets and the papillary muscles) are not rigid, but compliant, could help attenuate this error somewhat as well. As a result of this compliance, individual chordae can stretch relatively independent of each other and small changes in stiffness may result in changes in extension of that particular chordae, but might not significantly increase the overall force experienced by this chordae from coupling. As a result, small differences in stiffness of instrumented chordae may not propagate to an equally significant difference in force experienced by the instrumented chordae due to the mitigating effect tissue compliance has on mechanical coupling of chordae. Whether the effect of tissue compliance overcomes the effect of stiffness would likely vary depending on specific circumstances, and other researchers using similar sensing systems should verify that their particular setup minimizes error to an appropriate degree.

Left Heart Simulator. We designed a left heart model using computer-aided design software (Fusion 360, Autodesk, Inc., San Rafael, CA) and prototyped the device using additive manufacturing and machining technologies (Fig. 2(*a*)). The three-dimensional (3D)-printed left heart chamber (Carbon M2, Carbon3D, Inc., Redwood City, CA) was mounted to a programmable pulsatile linear piston pump (ViVitro Superpump, ViVitro Labs, Victoria, BC, Canada) with the ability to generate physiologic conditions using the pump controller and software (ViVitest Software, ViVitro Labs). The heart simulator was also outfitted with ventricular, aortic, left atrial, and coronary pressure transducers (Utah Medical Products, Inc., Midvale, UT), electromagnetic flow probes in the aortic and mitral positions (Carolina Medical Electronics, East Bend, NC), as well as a coronary flow probe (TS410 with 5PXN probe, Transonic Systems, Inc., Ithaca, NY). The linear actuator piston attaches to the ventricular chamber of the heart simulator with a modified pump-head attachment; the attachment uses a silicone membrane to separate the working fluid within the pump from the test fluid, protecting the pump from contamination and damage. We used 0.9% normal saline as a test fluid to ensure proper transduction of the electromagnetic flow meters.

A viscoelastic impedance adapter (ViVitro Labs), which consists of a 0–120 mL source air compliance chamber, a 0–60 mL output air compliance chamber, and a 200 dyne s/cm^5 fixed resistive element, was also outfitted to the heart simulator to reduce noise and generate more physiologic waveforms. In these experiments, we filled the source chamber with 100 mL of air and the output chamber with 50 mL of air. Compliance chambers in the aortic root and peripheral aortic position, with 500 mL total air volume each, were used to tune the waveform. Fluid from the venous reservoir enters the left atrial chamber via gravity, passes

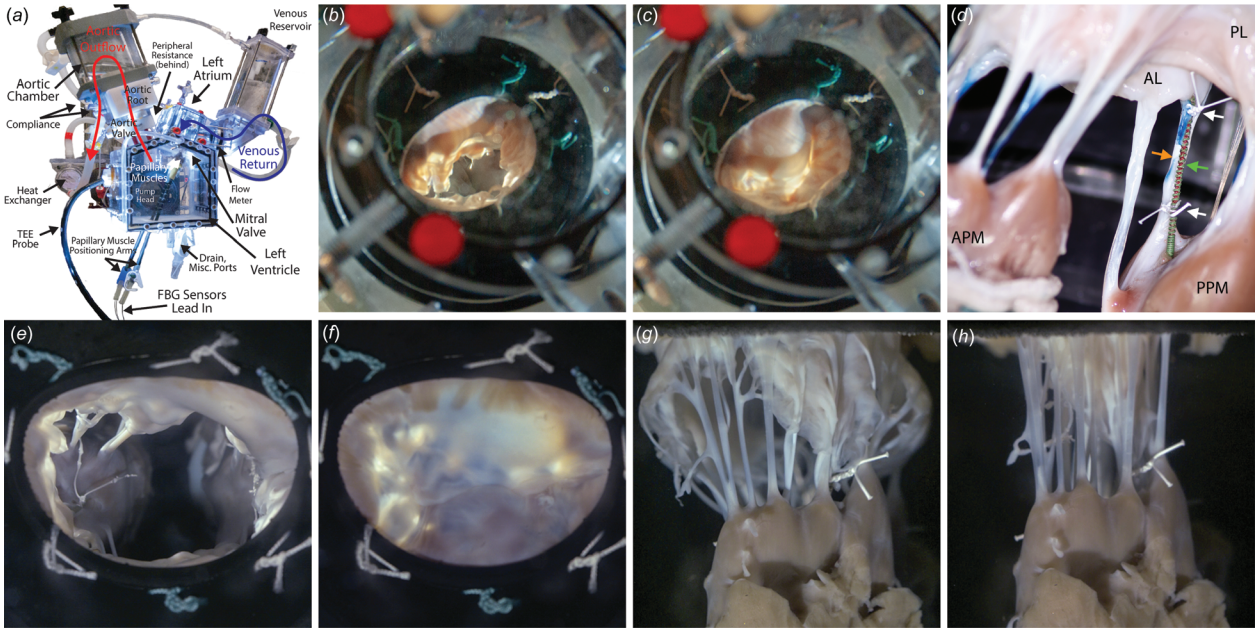

Fig. 2 Diagram of the left heart simulator (*a*) with each component labeled. Mitral valve tacked onto silicone sewing ring [43] (Reprinted with permission from Elsevier copyright 2019) ((*b*) and (*c*)) with interrupted sutures to obtain proper alignment. Final prototype of FSN implanted onto a mitral valve chordae tendineae (*d*) with the green arrow denoting the FSN, white arrows denoting the PTFE sutures attaching the chordae to the FSN proximally and distally to the sensor, and the orange arrow denoting the instrumented chordae. En face view of valves during diastole and systole ((*e*) and (*f*)). Lateral profile view of valves during diastole and systole ((*g*) and (*h*)). TEE: transesophageal echocardiography, FBG: fiber Bragg grating, APM: anterolateral papillary muscle, PPM: posteromedial papillary muscle, AL: anterior leaflet, and PL: posterior leaflet.

through the porcine mitral valve and into the ventricular chamber. The piston pressurizes the ventricular chamber, and fluid is ejected through the left ventricular outflow tract. After passing through the aortic flow probe and a mechanical aortic valve (29 mm St. Jude Regent, Abbott Laboratories, Chicago, IL), test fluid flows into the aortic root compliance chamber through a model aortic root and then into the aortic compliance assembly. Next, the test fluid is routed through a heat exchanger attached to an immersion circulator bath (PolyStat 3C15, Cole-Parmer, Vernon Hills, IL) to keep the test fluid at 37 °C, followed by a peripheral resistance throttle valve (ViVitro Labs), and finally back into the venous reservoir. To validate the system at baseline, a 28 mm leak-less disk valve (ViVitro Labs) in the mitral position was used.

The pump was programmed to generate an effective stroke volume of 70 mL/beat at 70 bpm, as measured by the flow meter. Next, peripheral resistance and compliance were titrated to generate a mean arterial pressure of 100 mmHg (systolic 120 mmHg, diastolic 80 mmHg) while keeping cardiac output at 5 liters per minute (LPM). A waveform complying with ISO 5840 standards for in vitro valve testing was used. The pressure transducers and flow meters were zeroed prior to every trial, and the baseline valve was reinstalled frequently between experimental trials to verify no drift had occurred.

Sample Preparation. Porcine hearts were obtained from a local abattoir and the mitral valves were excised, being careful to preserve the annulus, leaflets, and chordae. Some tertiary chordae attached to the ventricular wall did have to be cut while dissecting the valve, but all primary and secondary chordae were preserved. Only valves with intercommissural distances between 30 and 34 mm were used, and hearts with aberrant papillary muscle anatomy were excluded. A total of five valves were prepared and tested. A small cuff of left atrium was left in place and used to suture the mitral valve apparatus to a 3D-printed elastomeric polyurethane annular sewing plate (Carbon 3D) designed to fit between the left atrial and left ventricular chambers within the simulator (Figs. 2(*b*) and 2(*c*)). We attached the valve to the sewing ring using a cuff of left atrium rather than the annulus itself to better preserve native annular motion. The sewing ring itself was D-shaped to mimic the native mitral annulus, and the elastomeric material was chosen because it more closely matched the natural elasticity of the heart and held suture securely without tearing. Sewing rings were sized slightly larger (approximately 4 mm) than the native annulus of each valve to allow for an adequate cuff of left atrium attaching the valve apparatus to the elastomeric sewing ring and to prevent the sewing rings from restricting native annular motion. Importantly, because the native annulus is not rigidly attached directly to the sewing ring, its native motion and geometry are preserved, and it is free to conformationally change from saddle shape to flat during systole and diastole, respectively. Septolateral and transverse dimensions are also free to dynamically change throughout the cardiac cycle. 3D echocardiography was used to properly verify physiologic annular motion (Supplemental Video 1 available in the Supplemental Materials on the ASME Digital Collection). We used six to ten interrupted 2-0 braided polyester horizontal mattress sutures to tack the valve in place on the sewing ring for proper alignment. Next, a hemostatic suture line was used to attach the left atrial cuff to the underside of the sewing ring more securely using a continuous running 2-0 polypropylene suture; this suture line was locked to avoid a purse-string constriction effect resulting in an inadvertent restrictive annuloplasty. The papillary muscles were sewn to molded silicone papillary muscle holders using four interrupted, pledgeted, 2-0 braided polyester horizontal mattress sutures per papillary muscle. These sutures were carefully placed to avoid deforming or entangling any chordae insertion points. The papillary muscle holders were affixed to the ends of carbon fiber rods instrumented through a spherical compression gasket to allow movement in the x, y, and z axes.

Implementation of the Sensing Unit. The annular plate with valve attached was secured in the left heart simulator. The force-sensing neochordae were passed through the carbon fiber rods that

also served to position the papillary muscles using a modification of the Seldinger technique, allowing for quick sensor placement taking 5–10 min per chordae. We obtained 50 cm 14-gauge needles and sharpened them to a point. First, the needle was passed inferiorly through the papillary muscles—precisely at the insertion point of the chordae to be instrumented—and then passed through the silicone papillary muscle holders and carbon fiber papillary muscle positioning rods. Next, the sensors were passed superiorly through the needle until the sensor tip protruded through the proximal end of the needle. Holding the sensor fiber in position, the needle was carefully retracted superiorly over the sensor, leaving only the sensor passing through the papillary muscle, silicone papillary muscle holder, and carbon fiber positioning rod. The sensor was adjusted to the correct position relative to the chordae being instrumented by pulling superiorly or posteriorly and then locked into place. To lock the fibers into place without crushing them, we attached small segments of latex tubing to the proximal ends of the carbon fiber positioning rods, which the fibers also passed through. Plastic tubing clamps were carefully snapped into place once the fibers were in the correct position to prevent them from migrating during testing; the soft latex tubing not only cushioned the fibers to prevent crushing but also created a watertight seal. With the FSNs in the appropriate position, they were attached to the chordae of interest with PTFE suture, with the FSN being flanked on each side by a suture sewn to the respective chordae. To prevent the sensors from slipping, we first passed suture through the chordae, wrapping the suture around the chordae before securing it with a square knot. The sutures sewn to the chordae were then wrapped around the force-sensing neochord, taking care to ensure the suture was appropriately locked within one of the suture-locking grooves (Fig. 2(*d*)), and then secured with a series of square knots. Once attached, the segment of chordae between the sutures was cut so that the force-sensing neochord transmitted the full load of the chordae. This was repeated on all chordae of interest—in this case, several primary and secondary chordae on both anterior and posterior leaflets. Once the valve, papillary muscles, and FSNs were in place, the chamber was sealed and filled with 0.9% normal saline at 37 °C. Once filled, the papillary muscles were positioned anatomically with adequate coaptation of the mitral valve as determined visually, with echocardiography, and real-time flow measurements (Figs. 2(*e*)–2(*h*)); once fixed, movement of the papillary muscle positioning rods was minimized. The FSNs were zeroed to ensure only relative forces—above the native preloaded state of the chordae—were examined.

Data Acquisition and Analysis. After valves were mounted and FSNs were implanted, the system was filled with 37 °C normal saline, deaired, and allowed to run for 10 min prior to data collection. After 10 min, all sensors were zeroed and data collection began, which included pressure tracings, flow meter readings,

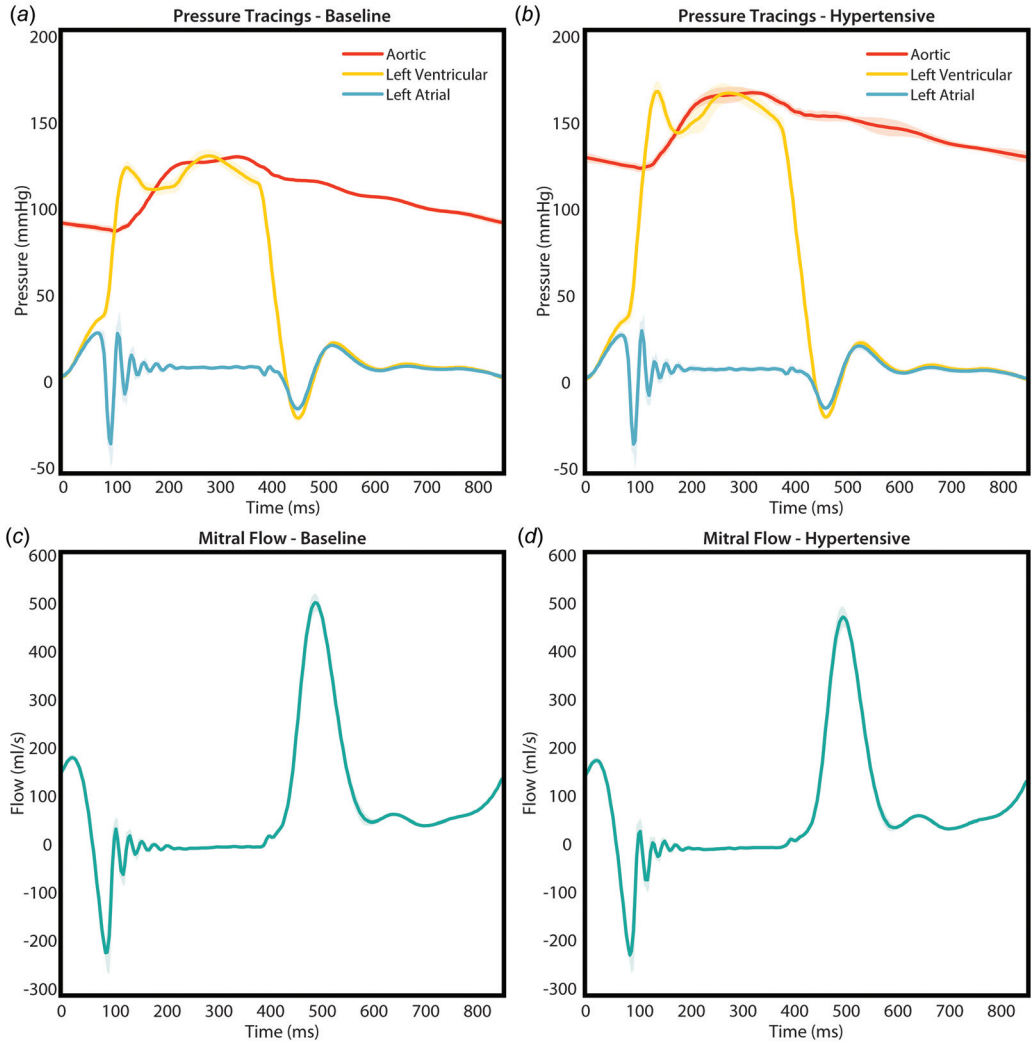

Fig. 3 Pressure tracings at baseline (*a*) and during hypertensive conditions (*b*) demonstrating physiologic characteristics. Flow tracings at baseline (*c*) and during hypertensive conditions (*d*).

Table 1 Hemodynamic and chordae tendineae tension parameters

	Baseline	Hypertension	*p*-value
Hemodynamics			
Annular diameter (mm)	32.00 ± 1.41	32.40 ± 1.67	0.621
Heart rate (bpm)	70.00 ± 0.00	70.00 ± 0.00	1.000
Mean arterial pressure (mmHg)	99.41 ± 0.96	135.78 ± 1.90	**<0.001**
Diastolic pressure (mmHg)	78.75 ± 1.84	114.06 ± 2.24	**<0.001**
Systolic pressure (mmHg)	120.79 ± 1.07	158.21 ± 2.94	**<0.001**
Mean atrial pressure (mmHg)	6.54 ± 1.17	5.66 ± 1.29	0.365
Mean ventricular pressure (mmHg)	50.11 ± 0.91	62.41 ± 1.79	**<0.001**
Cardiac output (liters/min)	4.55 ± 0.18	4.03 ± 0.21	**<0.001**
Effective stroke volume (ml)	64.99 ± 2.62	57.63 ± 2.99	**<0.001**
Pump stroke volume (ml)	109.74 ± 0.03	109.72 ± 0.05	0.466
Mitral valve mean gradient (mmHg)	4.85 ± 1.23	8.53 ± 0.64	**0.001**
Mitral valve mean back pressure (mmHg)	107.97 ± 3.99	143.38 ± 4.89	**<0.001**
Mitral forward flow time (s)	0.53 ± 0.01	0.53 ± 0.00	0.200
Mitral forward volume (ml/cycle)	69.90 ± 1.60	63.36 ± 2.12	**<0.001**
Mitral mean instantaneous flow (ml/cycle)	112.77 ± 2.60	101.06 ± 3.31	**<0.001**
Mitral RMS instantaneous flow (ml/cycle)	156.97 ± 4.45	143.70 ± 5.11	**<0.001**
Mitral peak instantaneous flow (ml/cycle)	427.02 ± 15.28	402.09 ± 17.03	**<0.001**
Effective orifice area (cm^2)	8.56 ± 2.09	8.57 ± 2.38	0.960
Mitral valve regurgitant fraction (%)	7.05 ± 2.25	9.06 ± 2.61	**0.006**
Mitral valve leakage rate (ml/s)	0.22 ± 3.11	2.56 ± 3.37	**0.014**
Mitral valve leakage volume (ml/cycle)	0.07 ± 0.89	0.70 ± 0.93	**0.015**
Mitral valve closing volume (ml/cycle)	4.98 ± 0.84	5.02 ± 0.85	0.403
Ventricular energy (mJ)	1156.21 ± 60.71	1460.02 ± 94.98	**<0.001**
Transmitral forward energy loss (mJ)	0.42 ± 5.63	−4.37 ± 6.79	**0.002**
Transmitral closing energy loss (mJ)	26.97 ± 3.69	27.03 ± 3.75	0.867
Transmitral leakage energy loss (mJ)	1.18 ± 12.71	15.60 ± 17.84	**0.021**
Transmitral total energy loss (mJ)	28.57 ± 18.42	38.27 ± 24.57	0.078
Chordae tendineae forces			
Anterior primary (N)	0.17 ± 0.08	0.23 ± 0.11	**0.004**
Anterior secondary (N)	0.74 ± 0.22	1.02 ± 0.38	**0.021**
Posterior primary (N)	0.12 ± 0.06	0.14 ± 0.07	**0.013**
Posterior secondary (N)	0.60 ± 0.26	0.78 ± 0.30	**0.026**

Data presented as mean ± standard deviation. RMS: root mean square. Bold denotes statistical significance ($p < 0.05$).

and force readings from the instrumented chordae. Data were exported into MATLAB (R2018a, Mathworks, Inc., Natick, MA) for plotting and into *R* for statistical analysis (R 3.6.0. with Jamovi 0.9.6.9 user interface). Continuous variables are reported as mean ± standard deviation (SD) unless otherwise noted. Nonparametric, paired-samples Wilcoxon tests were used to compare variables between the baseline and hypertensive conditions. A *p*-value of <0.05 was considered statistically significant.

Results

The 3D-printed left heart simulator generated physiologically representative pressure and flow waveforms, which are shown in Fig. 3 and detailed in Table 1. At baseline, mean arterial pressure was 99.41 ± 0.96 mmHg, systolic pressure was 120.79 ± 1.07 mmHg, and diastolic pressure was 78.75 ± 1.84 mmHg. Implantation of FSNs onto mitral valve chordae reliably generated high-fidelity force data with no obvious adverse effects on valve function or coaptation, with regurgitant fractions within normal ranges (7.07 ± 2.25%), most of which was closing volume. Echocardiographic data also verified normal leaflet and subvalvular apparatus kinematics. Up to six FSNs were implanted simultaneously on independent chordae with successful force measurement and no interference between sensors. Chordae tendineae forces are summarized at the bottom of Table 1 and shown graphically in Fig. 4. Our chordae force measurements are in agreement with reported values from the literature using various sensing techniques [28,32]. To verify functionality of the FSNs, the system pressure was increased to replicate hypertensive conditions with a mean arterial pressure of 135.78 ± 1.90 mmHg, systolic pressure of 158.21 ± 2.94 mmHg, and diastolic pressure of 114.06 ± 2.24 mmHg. Chordae tendineae forces in all positions were significantly elevated in the hypertensive condition, as were several hemodynamic parameters as summarized in Table 1. Specifically, forces at baseline and hypertensive conditions for anterior primary chordae were 0.17 ± 0.08 N versus 0.23 ± 0.11 N ($p = 0.004$). Posterior primary chordae tendineae forces at baseline were 0.12 ± 0.06 versus 0.14 ± 0.07 N ($p = 0.013$) during hypertensive conditions. For anterior secondary chordae, baseline forces were 0.74 ± 0.22 versus 1.02 ± 0.38 N during hypertensive conditions ($p = 0.021$) and 0.60 ± 0.26 versus 0.78 ± 0.30 N ($p = 0.026$) for posterior secondary forces at baseline and during hypertensive conditions, respectively. Forces on secondary chordae appeared to increase to a higher degree in response to increased pressure as opposed to primary chordae, which were less impacted. Early trials did have isolated instances of the FSNs becoming detached from the chordae, which was solved by increasing the size of the PTFE suture or using a figure-of-eight attachment suture on the chordae prior to tying the FSN in place. None of the FSNs, once implanted, failed or ruptured during testing.

Discussion

The results of our study demonstrate that FBG optical sensors can be successfully incorporated into devices to measure multiple simultaneous mitral valve chordae tendineae forces with a high degree of sensitivity and reproducibility, while overcoming some limitations of earlier technology. In addition, the small footprint of FBGs allows forces on multiple chordae to be simultaneously measured, which is challenging with bulkier sensors. In addition, their small size and weight also minimize the impact the sensor has on the structures being measured. Furthermore, FBG-based sensors are waterproof and robust in the tensile direction of force

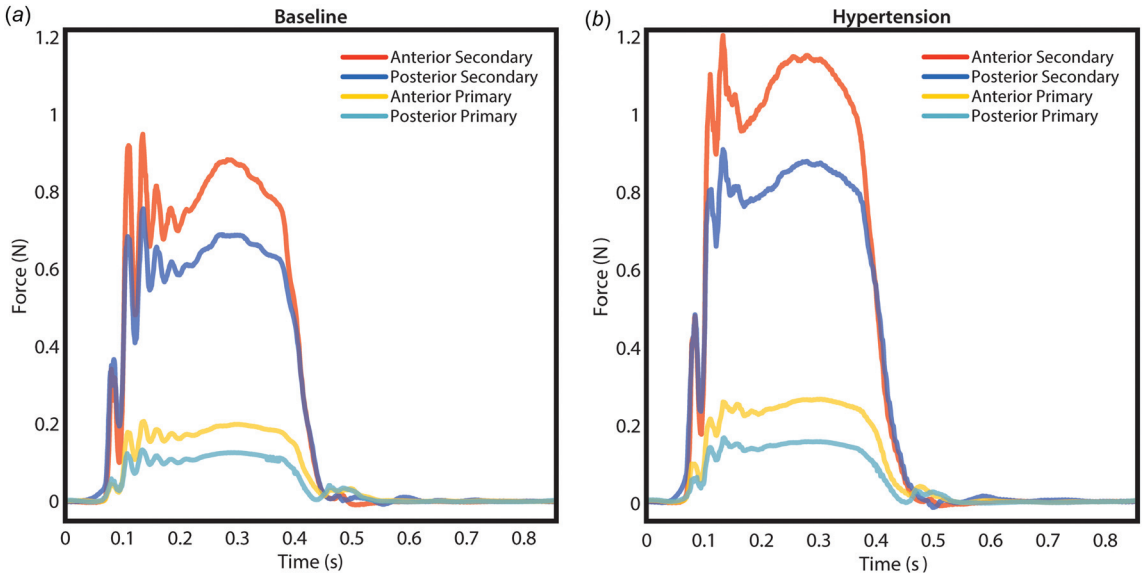

Fig. 4 Chordae tendineae force tracings at baseline (*a*) and during hypertensive conditions (*b*) demonstrating high fidelity force readings at a temporal resolution of 1000 Hz. Secondary chordae appeared to increase more significantly in response to increases in pressure.

measurement. Electromagnetic fields do not interfere with FBG measurements, allowing them to be used in a variety of clinical environments, including during MRI.

In addition to measuring chordae tendineae forces, the versatility of FBGs could easily allow for measurements of more complex structures within the heart and body. Novel applications using FBGs include providing haptic feedback of needles, catheters, and robotic arms allowing for enhanced surgical manipulation as well as for diagnostics in the case of force-sensing needles for tumor biopsy [36–38]. We are currently experimenting with force and shape-sensing annuloplasty rings using multicore and bundled fibers oriented at 120 deg angles. Based on relative elongation and compression, shape can be deduced from FBG readings. Their use is also not limited to in vitro applications. The inert nature of silica-based FBG fibers makes them ideal for in vivo applications as they are not expected to cause significant tissue reactivity.

In this manuscript, it is important to note that a planar annular model was used for simplicity, as our aim was to focus primarily on the measurement technology. As a multitude of studies on various annular conformations have clearly demonstrated, annular geometry and material properties exert pronounced effects on chordae tension and valvular function [27,31,39–42]. The sensing technology we describe can be used in a range of other in vitro and in vivo annular models, and is an important future step.

While FBGs overcome some issues that have faced prior measurement strategies, they are not without limitations. For one, the associated equipment is costly, and the individual fibers are expensive. Additionally, fabrication requires a multiple-week lead time and calibration can be time-intensive. We have begun using an Instron 5848 Microtester (Illinois Tool Works, Inc.) with a 20 N load cell to perform automated tensioning cycles to increase calibration accuracy and speed. While silica-based FBGs have tremendous tensile strength, they are prone to breaking if bent past their maximum radius of curvature or if crushed (in a vessel clip, for example, which we experimented with unsuccessfully in lieu of sutures to make the mounting process quicker). The peak wavelength measurements can widen or split when the sensors are subjected to nonuniaxial loading; this is particularly important for the proposed technique because it necessitates careful attachment to the chordae to ensure the FBG is pulled only along its longitudinal axis. They are also prone to a "whip" phenomenon if they are not secured proximally, which is why we chose to run the fibers within the papillary muscle mounting rods and not freely floating in the ventricular chamber. In addition, naked fibers can be difficult to see, so inadvertently cutting them along with the chordae being instrumented can occur and is a costly mistake. Though we are working to manufacture shorter fibers that replace a smaller fraction of the native chordae (and thus better retaining the native chordae's viscoelastic response), the current disparity in stiffness between the native and instrumented chordae can result in measurement error and represents an important limitation in our technique. Polymer-based fibers will solve many of the limitations of silica-based FBGs, including more closely matching the material properties of native chordae tendineae to reduce error due to the sensor replacing a segment of native chordae. These polymer-based FBGs have been developed in several laboratories globally but are not yet available commercially. In addition, polymeric FBGs will be substantially more robust and flexible, allowing for further development of novel biological and clinical sensing systems.

Conclusions

Using fiber Bragg grating optical strain gauges, a novel device created to measure mitral valve chordae tendineae tension was successfully developed, tested, and validated. This new force-sensing device, with its small physical footprint and high fidelity, allows for measurement of multiple chordae simultaneously with minimal interference on leaflet or chordae kinematics.

Funding Data

- National Institutes of Health (Grant No. NIH R01 HL089315-01, YJW, Funder ID: 10.13039/100000002).
- American Heart Association (Grant Nos. AHA 17POST33410497, MJP and AHA 18POST33990223, HW, Funder ID: 10.13039/100000968).
- National Science Foundation Graduate Research Fellowship Program (AMI) (Grant No. GRFP-DGE-1656518, Funder ID: 10.13039/501100008982).
- Stanford Graduate Fellowship (AMI).

References

[1] Mozaffarian, D., Benjamin, E. J., Go, A. S., Arnett, D. K., Blaha, M. J., Cushman, M., de Ferranti, S., Després, J.-P., Fullerton, H. J., Howard, V. J., Huffman, M. D., Judd, S. E., Kissela, B. M., Lackland, D. T., Lichtman, J. H.,

Lisabeth, L. D., Liu, S., Mackey, R. H., Matchar, D. B., McGuire, D. K., Mohler, E. R., Moy, C. S., Muntner, P., Mussolino, M. E., Nasir, K., Neumar, R. W., Nichol, G., Palaniappan, L., Pandey, D. K., Reeves, M. J., Rodriguez, C. J., Sorlie, P. D., Stein, J., Towfighi, A., Turan, T. N., Virani, S. S., Willey, J. Z., Woo, D., Yeh, R. W., and Turner, M. B., and American Heart Association Statistics Committee and Stroke Statistics Subcommittee, 2015, "Heart Disease and Stroke Statistics–2015 Update: A Report From the American Heart Association," Circulation, **131**(4), pp. e29–e322.

[2] Devereux, R. B., Jones, E. C., Roman, M. J., Howard, B. V., Fabsitz, R. R., Liu, J. E., Palmieri, V., Welty, T. K., and Lee, E. T., 2001, "Prevalence and Correlates of Mitral Valve Prolapse in a Population-Based Sample of American Indians: The Strong Heart Study," Am. J. Med., **111**(9), pp. 679–685.

[3] Freed, L. A., Levy, D., Levine, R. A., Larson, M. G., Evans, J. C., Fuller, D. L., Lehman, B., and Benjamin, E. J., 1999, "Prevalence and Clinical Outcome of Mitral-Valve Prolapse," N. Engl. J. Med., **341**(1), pp. 1–7.

[4] de Marchena, E., Badiye, A., Robalino, G., Junttila, J., Atapattu, S., Nakamura, M., De Canniere, D., and Salerno, T., 2011, "Respective Prevalence of the Different Carpentier Classes of Mitral Regurgitation: A Stepping Stone for Future Therapeutic Research and Development," J. Card. Surg., **26**(4), pp. 385–392.

[5] Hayek, E., Gring, C. N., and Griffin, B. P., 2005, "Mitral Valve Prolapse," Lancet, **365**(9458), pp. 507–518.

[6] Nishimura, R. A., McGoon, M. D., Shub, C., Miller, F. A., Ilstrup, D. M., and Tajik, A. J., 1985, "Echocardiographically Documented Mitral-Valve Prolapse. Long-Term Follow-Up of 237 Patients," N. Engl. J. Med., **313**(21), pp. 1305–1309.

[7] Mills, P., Rose, J., Hollingsworth, J., Amara, I., and Craige, E., 1977, "Long-Term Prognosis of Mitral-Valve Prolapse," N. Engl. J. Med., **297**(1), pp. 13–18.

[8] Düren, D. R., Becker, A. E., and Dunning, A. J., 1988, "Long-Term Follow-Up of Idiopathic Mitral Valve Prolapse in 300 Patients: A Prospective Study," J. Am. Coll. Cardiol., **11**(1), pp. 42–47.

[9] St John Sutton, M., and Weyman, A. E., 2002, "Mitral Valve Prolapse Prevalence and Complications: An Ongoing Dialogue," Circulation, **106**(11), pp. 1305–1307.

[10] Goldstone, A. B., Cohen, J. E., Howard, J. L., Edwards, B. B., Acker, A. L., Hiesinger, W., MacArthur, J. W., Atluri, P., and Woo, Y. J., 2015, "A "Repair-All" Strategy for Degenerative Mitral Valve Disease Safely Minimizes Unnecessary Replacement," Ann. Thorac. Surg., **99**(6), pp. 1983–1990.

[11] Gillinov, A. M., Blackstone, E. H., Nowicki, E. R., Slisatkorn, W., Al-Dossari, G., Johnston, D. R., George, K. M., Houghtaling, P. L., Griffin, B., Sabik, J. F., and Svensson, L. G., 2008, "Valve Repair Versus Valve Replacement for Degenerative Mitral Valve Disease," J. Thorac. Cardiovasc. Surg., **135**(4), pp. 885–893.

[12] Cohn, L. H., Couper, G. S., Aranki, S. F., Rizzo, R. J., Kinchla, N. M., and Collins, J. J., 1994, "Long-Term Results of Mitral Valve Reconstruction for Regurgitation of the Myxomatous Mitral Valve," J. Thorac. Cardiovasc. Surg., **107**(1), pp. 143–150.

[13] David, T. E., Ivanov, J., Armstrong, S., Feindel, C. M., and Cohen, G., 2001, "Late Results of Heart Valve Replacement With the Hancock II Bioprosthesis," J. Thorac. Cardiovasc. Surg., **121**(2), pp. 268–277.

[14] Lee, E. M., Shapiro, L. M., and Wells, F. C., 1997, "Superiority of Mitral Valve Repair in Surgery for Degenerative Mitral Regurgitation," Eur. Heart J., **18**(4), pp. 655–663.

[15] Enriquez-Sarano, M., Schaff, H. V., Orszulak, T. A., Tajik, A. J., Bailey, K. R., and Frye, R. L., 1995, "Valve Repair Improves the Outcome of Surgery for Mitral Regurgitation. A Multivariate Analysis," Circulation, **91**(4), pp. 1022–1028.

[16] Goldstone, A. B., Patrick, W. L., Cohen, J. E., Aribeana, C. N., Popat, R., and Woo, Y. J., 2015, "Early Surgical Intervention or Watchful Waiting for the Management of Asymptomatic Mitral Regurgitation: A Systematic Review and Meta-Analysis," Ann. Cardiothorac. Surg., **4**(3), pp. 220–229.

[17] Savage, E. B., Ferguson, T. B., and DiSesa, V. J., 2003, "Use of Mitral Valve Repair: Analysis of Contemporary United States Experience Reported to the Society of Thoracic Surgeons National Cardiac Database," Ann. Thorac. Surg., **75**(3), pp. 820–825.

[18] Gammie, J. S., Sheng, S., Griffith, B. P., Peterson, E. D., Rankin, J. S., O'Brien, S. M., and Brown, J. M., 2009, "Trends in Mitral Valve Surgery in the United States: Results From the Society of Thoracic Surgeons Adult Cardiac Surgery Database," Ann. Thorac. Surg., **87**(5), pp. 1431–1437.

[19] Pouch, A. M., Jackson, B. M., Lai, E., Takebe, M., Tian, S., Cheung, A. T., Woo, Y. J., Patel, P. A., Wang, H., Yushkevich, P. A., Gorman, R. C., and Gorman, J. H., 2016, "Modeling the Myxomatous Mitral Valve With Three-Dimensional Echocardiography," Ann. Thorac. Surg., **102**(3), pp. 703–710.

[20] Vergnat, M., Jackson, B. M., Cheung, A. T., Weiss, S. J., Ratcliffe, S. J., Gillespie, M. J., Woo, Y. J., Bavaria, J. E., Acker, M. A., Gorman, R. C., and Gorman, J. H., 2011, "Saddle-Shape Annuloplasty Increases Mitral Leaflet Coaptation After Repair for Flail Posterior Leaflet," Ann. Thorac. Surg., **92**(3), pp. 797–803.

[21] Vergnat, M., Levack, M. M., Jassar, A. S., Jackson, B. M., Acker, M. A., Woo, Y. J., Gorman, R. C., and Gorman, J. H., 2012, "The Influence of Saddle-Shaped Annuloplasty on Leaflet Curvature in Patients With Ischaemic Mitral Regurgitation," Eur. J. Cardiothorac. Surg., **42**(3), pp. 493–499.

[22] Bouma, W., Lai, E. K., Levack, M. M., Shang, E. K., Pouch, A. M., Eperjesi, T. J., Plappert, T. J., Yushkevich, P. A., Mariani, M. A., Khabbaz, K. R., Gleason, T. G., Mahmood, F., Acker, M. A., Woo, Y. J., Cheung, A. T., Jackson, B. M., Gorman, J. H., and Gorman, R. C., 2016, "Preoperative Three-Dimensional Valve Analysis Predicts Recurrent Ischemic Mitral Regurgitation After Mitral Annuloplasty," Ann. Thorac. Surg., **101**(2), pp. 567–575.

[23] Levack, M. M., Jassar, A. S., Shang, E. K., Vergnat, M., Woo, Y. J., Acker, M. A., Jackson, B. M., Gorman, J. H., and Gorman, R. C., 2012, "Three-Dimensional Echocardiographic Analysis of Mitral Annular Dynamics: Implication for Annuloplasty Selection," Circulation, **126**(11_suppl_1), p. S183.

[24] Nielsen, S. L., Nygaard, H., Fontaine, A. A., Hasenkam, J. M., He, S., Andersen, N. T., and Yoganathan, A. P., 1999, "Chordal Force Distribution Determines Systolic Mitral Leaflet Configuration and Severity of Functional Mitral Regurgitation," J. Am. Coll. Cardiol., **33**(3), pp. 843–853.

[25] Jensen, M. O., Fontaine, A. A., and Yoganathan, A. P., 2001, "Improved In Vitro Quantification of the Force Exerted by the Papillary Muscle on the Left Ventricular Wall: Three-Dimensional Force Vector Measurement System," Ann. Biomed. Eng., **29**(5), pp. 406–413.

[26] Lomholt, M., Nielsen, S. L., Hansen, S. B., Andersen, N. T., and Hasenkam, J. M., 2002, "Differential Tension Between Secondary and Primary Mitral Chordae in an Acute In-Vivo Porcine Model," J. Heart Valve Dis., **11**(3), pp. 337–345.

[27] Jimenez, J. H., Soerensen, D. D., He, Z., He, S., and Yoganathan, A. P., 2003, "Effects of a Saddle Shaped Annulus on Mitral Valve Function and Chordal Force Distribution: An In Vitro Study," Ann. Biomed. Eng., **31**(10), pp. 1171–1181.

[28] Nielsen, S. L., Soerensen, D. D., Libergren, P., Yoganathan, A. P., and Nygaard, H., 2004, "Miniature C-Shaped Transducers for Chordae Tendineae Force Measurements," Ann. Biomed. Eng., **32**(8), pp. 1050–1057.

[29] Nielsen, S. L., Hansen, S. B., Nielsen, K. O., Nygaard, H., Paulsen, P. K., and Hasenkam, J. M., 2005, "Imbalanced Chordal Force Distribution Causes Acute Ischemic Mitral Regurgitation: Mechanistic Insights From Chordae Tendineae Force Measurements in Pigs," J. Thorac. Cardiovasc. Surg., **129**(3), pp. 525–531.

[30] Jimenez, J. H., Soerensen, D. D., He, Z., Ritchie, J., and Yoganathan, A. P., 2005, "Effects of Papillary Muscle Position on Chordal Force Distribution: An In-Vitro Study," J. Heart Valve Dis., **14**(3), pp. 295–302.

[31] Jimenez, J. H., Soerensen, D. D., He, Z., Ritchie, J., and Yoganathan, A. P., 2005, "Mitral Valve Function and Chordal Force Distribution Using a Flexible Annulus Model: An In Vitro Study," Ann. Biomed. Eng., **33**(5), pp. 557–566.

[32] He, Z., and Jowers, C., 2009, "A Novel Method to Measure Mitral Valve Chordal Tension," ASME J. Biomech. Eng., **131**(1), p. 014501.

[33] Tosi, D., Olivero, M., and Perrone, G., 2008, "Low-Cost Fiber Bragg Grating-Based Static and Dynamic Strain System for Structural Monitoring," Eighth International Conference on Vibration Measurements by Laser Techniques: Advances and Applications, Ancona, Italy, 2008, p. 70981G.

[34] Cochran, R. P., and Kunzelman, K. S., 1991, "Comparison of Viscoelastic Properties of Suture Versus Porcine Mitral Valve Chordae Tendineae," J. Card. Surg., **6**(4), pp. 508–513.

[35] Lim, K. O., and Boughner, D. R., 1975, "Mechanical Properties of Human Mitral Valve Chordae Tendineae: Variation With Size and Strain Rate," Can. J. Physiol. Pharmacol., **53**(3), pp. 330–339.

[36] Elayaperumal, S., Bae, J. H., Christensen, D., Cutkosky, M. R., Daniel, B. L., Costa, J. M., Black, R. J., Faridian, F., and Moslehi, B., 2013, "MR-Compatible Biopsy Needle With Enhanced Tip Force Sensing," Joint Eurohaptics Conference and Symposium on Haptic Interfaces Virtual Environment and Teleoperator Systems, Daejeon, South Korea, 2013, pp. 109–114.

[37] Elayaperumal, S., Bae, J. H., Daniel, B. L., and Cutkosky, M. R., 2014, "Detection of Membrane Puncture With Haptic Feedback Using a Tip-Force Sensing Needle," IEEE/RSJ International Conference on Intelligent Robots and Systems, Chicago, IL, 2014, pp. 3975–3981.

[38] Park, Y.-L., Chau, K., Black, R. J., and Cutkosky, M. R., 2007, "Force Sensing Robot Fingers Using Embedded Fiber Bragg Grating Sensors and Shape Deposition Manufacturing," IEEE International Conference on Robotics and Automation, Roma, Italy, 2007, pp. 1510–1516.

[39] Eckert, C. E., Zubiate, B., Vergnat, M., Gorman, J. H., Gorman, R. C., and Sacks, M. S., 2009, "In Vivo Dynamic Deformation of the Mitral Valve Annulus," Ann. Biomed. Eng., **37**(9), pp. 1757–1771.

[40] Jensen, M. O., Jensen, H., Levine, R. A., Yoganathan, A. P., Andersen, N. T., Nygaard, H., Hasenkam, J. M., and Nielsen, S. L., 2011, "Saddle-Shaped Mitral Valve Annuloplasty Rings Improve Leaflet Coaptation Geometry," J. Thorac. Cardiovasc. Surg., **142**(3), pp. 697–703.

[41] Ritchie, J., Jimenez, J., He, Z., Sacks, M. S., and Yoganathan, A. P., 2006, "The Material Properties of the Native Porcine Mitral Valve Chordae Tendineae: An In Vitro Investigation," J. Biomech., **39**(6), pp. 1129–1135.

[42] Amini, R., Eckert, C. E., Koomalsingh, K., McGarvey, J., Minakawa, M., Gorman, J. H., Gorman, R. C., and Sacks, M. S., 2012, "On the In Vivo Deformation of the Mitral Valve Anterior Leaflet: Effects of Annular Geometry and Referential Configuration," Ann. Biomed. Eng., **40**(7), pp. 1455–1467.

[43] Imbrie-Moore, A. M., Paulsen, M. J., Thakore, A. D., Wang, H., Hironaka, C. E., Lucian, H. J., Farry, J. M., Edwards, B. B., Bae, J. H., Cutkosky, M. R., and Woo, Y. J., 2019, "Ex Vivo Biomechanical Study of Apical Versus Papillary Neochord Anchoring for Mitral Regurgitation," Ann Thorac Surg., **108**(1), pp. 90–97.